Supporting Information for

Electrowetting-Dominated Instability of Cassie Droplets on Superlyophobic Pillared Surfaces

Yu-Chung Chen, Yuji Suzuki, and Kenichi Morimoto*

Department of Mechanical Engineering, The University of Tokyo,

7-3-1 Hongo, Bunkyo-ku, Tokyo 113-8656, Japan

*morimoto@mesl.t.u-tokyo.ac.jp

Contents:

Details of the Fabrication Process and Geometrical Parameters

Figure S1 shows the MEMS-based fabrication processes of the present surfaces: (a) SU-8 pillars, (b) CYTOP pillars, and (c) Si/SiO_2 pillars.

For SU-8 pillars, a glass wafer is first sputtered with 200 nm thick ITO. 45 μm thick SU-8 (SU-8 2075, MicroChem Corp.) is spin-coated onto the surface. The SU-8 is patterned with UV-exposure in the mask aligner (MA6-8, SUSS MicroTec, GmbH) and developed with SU-8 developer. The pillars are then deposited with PFOTS layer.

For CYTOP pillars, around 15 μm thick CYTOP CTL-M (Asahi Glass Co., Ltd.) is spin-coated onto a Si wafer. 350 nm thick Cu layer is sputtered on top of the CYTOP. The photolithography is processed using the AZP-4400 photoresist with UV-exposure and developed with AZ developer 400K. The Cu pattern is formed with wet etching solution (citric acid: H_2O_2: H_2O = 4: 1: 16, w/w). The photoresist is then removed by AZ remover-700. The pillar is formed through magnetron plasma etching (TEP-Xd, Tateyama Machine Co., Ltd.) using a Cu mask. After removing the Cu with Cu etchant, the pillar is annealed at 180 ºC for 10 min to promote hydrophobicity.

For Si/SiO_2 pillars, 300 nm thick SiO_2 is formed on the top with wet oxidation in 1050 ºC oxidation furnace. OEBR-CAP112 photoresist is spin-coated and exposed by electron beam (F5112+VD01, Advantest, Co.). The pattern is formed with development in NMD-3 (TMAH 2.38%) developer. ICP-RIE (CE-300I, ULVAC, Co., Inc.) with CHF_3 plasma is applied to etch the SiO_2. The Bosch process is applied in the DRIE process (MUC-21, SPP Technology Co., Ltd.) to further etch the Si and form the pillar shape. The etching/passivation time per cycle is adjusted to have larger side etching effect on Si. The different etching rate between Si and SiO_2 forms the overhanging structure on top of the pillar. Through further oxidization, 670 nm thick SiO_2 is formed on the pillar side wall and bottom surface. The SiO_2 on the backside of pillar surface is removed with BHF to reveal the conductive Si. The surface is then covered with the monolayer of 1H,1H,2H,2H-Perfluoro-octyltrichlorosilane (PFOTS, Wako Pure Chemical Industries, Ltd.) using vapor deposition.

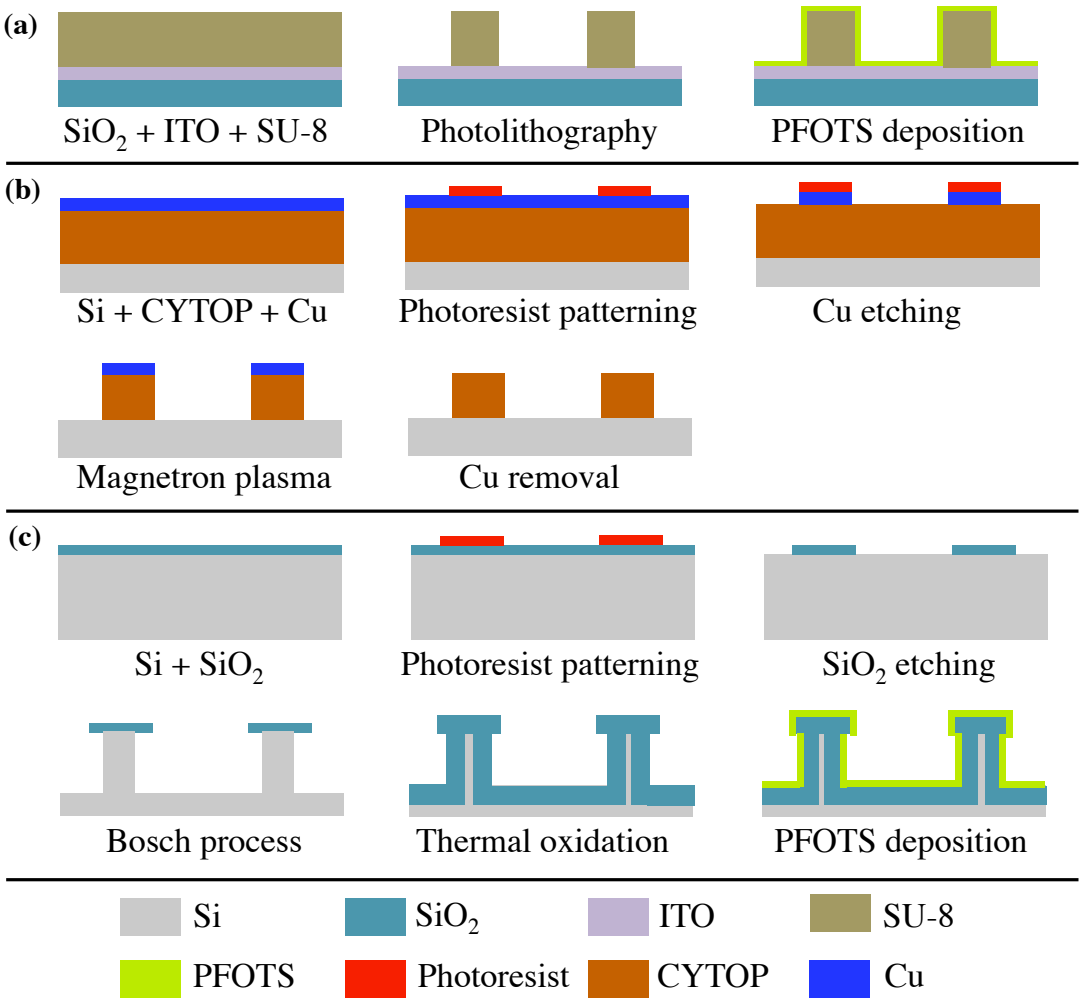

Figure S1. MEMS-based fabrication processes: (a) SU-8 pillars, (b) CYTOP pillars, and (c) Si/SiO_2 pillars.

Table S1. Geometrical parameters for the present pillared surfaces.

	Pitch, P [μm]	Diameter, D [μm]	Height, H [μm]	Solid Fraction, f_S	Overhanging Length [μm]	t^* (H/P)
SU-8	80	15.7	43.2	0.030		0.54
CYTOP	40	8.3	15.2	0.033		0.38
	20	8.5	14.6	0.14		0.73
	24	2.6	14.5	0.0091		0.60
	12	2.5	14.8	0.034		1.23
Si/SiO_2	80	9.3	25.1	0.011	2.22	0.31
		9.3	34.6	0.011	3.05	0.43
		9.2	42.5	0.010	2.94	0.53
		9.2	51.9	0.010	2.57	0.65
		9.2	72.3	0.010	2.85	0.90

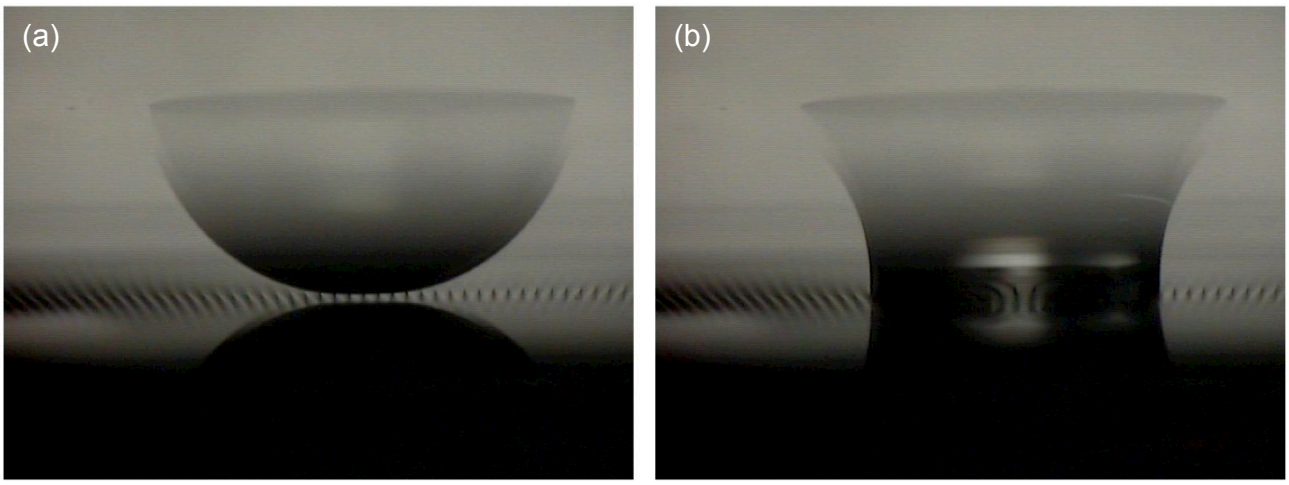

Figure S2. Snapshot images of glycerol dropltes on Si/SiO2 pillar with (P, D, H) = (80, 9.3, 25.1 μm): (a) Cassie state without applied voltage, and (b) Collapsed at the critical voltage of 72 V.

Figure S2 shows snapshot images of glycerol dropltes on Si/SiO2 pillar with (P, D, H) = (80, 9.3, 25.1 μm). As shown in Figure S2a, the liquid droplets sit on the present surfaces are in the Cassie state under no applied voltage, and the transition to the Wenzel state is observed under

elevated voltage as in Figure S2b. In certain ranges of the pillar configuration, the Laplace pressure corresponding to the macroscale droplet shape might change under the electric field [25], and the apparent contact angle decreases with increasing voltage [26]. In the present pillar geometry, on the other hand, the shape of the Cassie droplet does not change significantly before collapsing to the Wenzel state. Thus, the effect of the droplet shape on the Laplace pressure is considered to be negligible if compared to the effect of the electric field.

Details of the Numerical Simulation

Figure S3 shows the convergence history for V and h with a given condition of dielectric pillars with (P, D, H) = (80, 15.7, 43.2 μm). The applied voltage is 140 V on glycerol with a constant pressure of 100 Pa. The rate of change per one loop of the present iterative simulation is defined as: $\sum_{i,j,k=0}^{N} \frac{|V_{update} - V_{privious}|}{V_{Applied}}$ for electric potential and $\sum_{i,j=0}^{N} \frac{|h_{update} - h_{privious}|}{H}$ for the liquid-air interface. It is seen that the rate of change decreases rapidly and reaches the machine epsilon of double precision, 2.22×10^{-16} and/or stops decreasing at certain value. The electric potential is judged to be converged when the change per loop reaches 1.86×10^{-3} at the loop number of 4669. The electric force only differs around 0.01 nN if further iteration reaches the machine epsilon at the loop number of 14860. The liquid-air interface is judged to be converged when the change per loops reaches 7.3×10^{-5} at the loop number of 16675, and the deformation differs within 0.01 μm if further iteration proceeds up to 75000 loops. Figure 2(c) shows the deformation dependence on the number of grids, which is set to be the same for x-, y- and z- directions. The deformation decreases from -3.9 μm at 10 grids to around -3.3 μm when increasing up to 200 grids. The present data applies 40 grids in the simulation, which differs around 0.06 μm with the results of 200 grids. The errors from the iteration residuals and finite grid numbers are negligible comparing to the deviation with experimental scanning curve, which is at the level of 1 μm. The previously reported simulation by Oh *et al*. [21] is reproducible in the present iterative calculation given the same geometrical condition.

Figure S4 shows the determination process of the critical voltage in the simulation. As the voltage increases, the height of the liquid-air interface gradually decreases while the CA increases. The solution of the liquid-air interface profile is obtained until the pull-in voltage of 223 V, where h_C suddenly diminishes due to the electrostatic instability [24]. In the present analysis, it is assumed

that the slide-down motion is triggered when the CA at the pillar edge comes across the maximum advancing CA at 165 V. If the simulated CA does not reach the advancing CA before the pull-in limit, the slide-down voltage cannot be determined and the critical voltage corresponds to the pull-in voltage.

It is noted that the voltage for the CA to reach the maximum advancing CA is related with the pitch, diameter and height of the pillars. The maximum advancing CA that is reduced by the electrowetting, and the deformation of liquid-air interface due to the electric field are both dependent on the geometry. Smaller pitch and larger height and diameter will have larger resistance from surface tension to the electrostatic deformation, so that larger voltage is needed to the slide down. Also the determination of CA at the pillar edge is dependent on the shape of the edge. When the maximum advancing CA becomes smaller than the initial CA without voltage, the slide-down voltage becomes irrelevant with geometry [36].

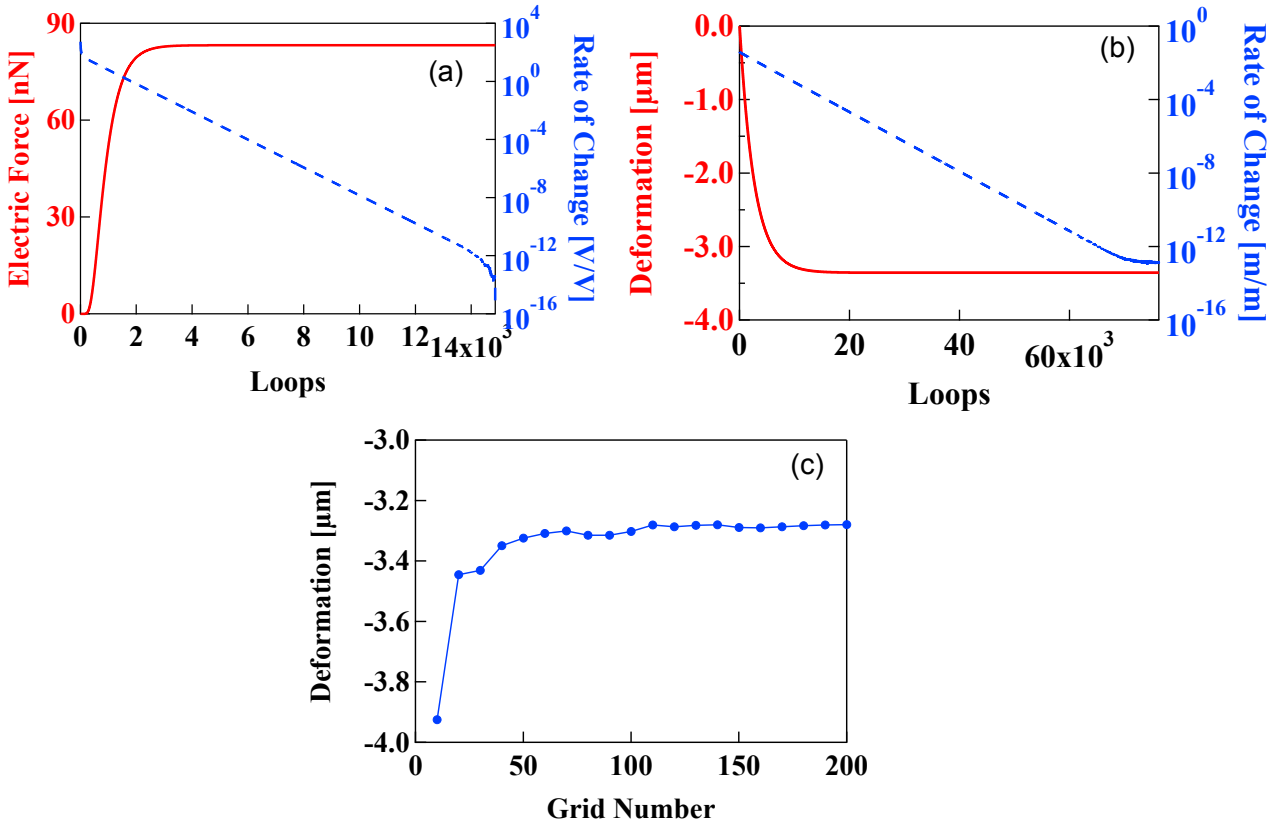

Figure S3. The convergence nature and grid-number independency of the present simulation: (a) The electric force and rate of change dependence on the loops in iteration for V, (b) The deformation and rate of change, and (c) Grid number dependency of the simulated deformation.

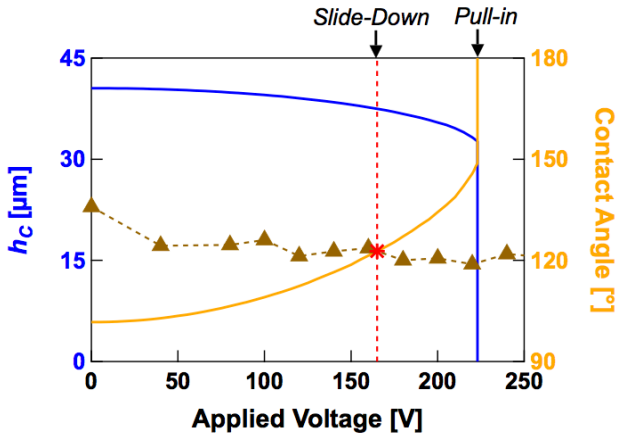

Figure S4. Determination of the critical voltage in the present simulation. The data for water on Si/SiO_2 pillar with (P, D, H) = (80, 9.2, 42.8 μm) are shown here. The blue line is the central-point deformation. The yellow line is the CA at the pillar edge, and the triangle marker is the advancing CA measured on flat Si/SiO_2 with PFOTS deposition. The pull-in and the slide-down voltages are estimated to be 223 V and 165 V, respectively.

Simulation results of the 3-D liquid-air interface profile

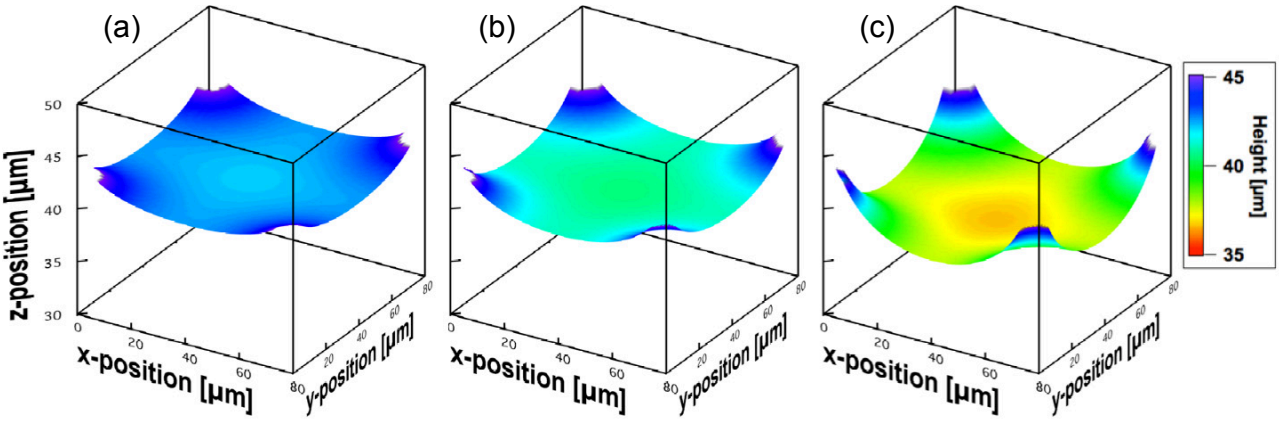

Figure S5. Profiles of the liquid-air interface obtained from the present simulation for glycerol droplets on SU-8 pillar with (P, D, H) = (80, 15.7, 43.2 μm) under the applied voltage of (a) 0 V, (b) 140 V, and (c) 240 V.

Table S2. Data for the central-point deformation $H - h_C$ and the contact angle under applied voltage on SU-8 pillar with (P, D, H) = (80, 15.7, 43.2 μm) from the scanned curve and the simulation. The CA estimated from eq. 6 is listed in the "Model" column.

Applied voltage [V]	Deformation ($H - h_C$) [μm]		Contact angle [º]		
	Scanned	Simulation	Scanned	Simulation	Model
0	1.94	1.93	99.5	100.2	96.9
140	3.26	2.94	101.2	105.6	101.5
240	6.61	5.41	112.4	118.7	112.4

Table S3. Data for the central-point deformation $H - h_C$ and the contact angle of water, glycerol, and hexadecane droplets on superlyophobic Si/SiO_2 pillar with (P, D, H) = (80, 9.2, 42.8 μm) from the scanned curve and the simulation. The CA estimated from eq. 6 is listed in the "Model" column.

Liquid type	Applied voltage [V]	Deformation ($H - h_C$) [μm]		Contact angle (θ_0) [º]		
		Scanned	Simulation	Scanned	Simulation	Model
Water	0	1.85	1.81	97.2	100.6	96.0
	160	6.24	4.91	110.9	124.1	109.4
Glycerol	0	2.49	2.41	99.8	104.1	98.0
	140	5.18	5.21	106.1	124.3	106.3
Hexadecane	0	2.77	2.90	102.2	107.1	98.9
	85	6.63	5.69	110.2	128.4	110.5